Photo-thermo synergistic permanganate decomposition over a hydrolytically stable Co(II)-MOF

Quan-Quan Li,[a] Huan-Xi Wang,[b] Yi Deng,[b] Si-Yu Chen,[a] Yang Chen,[a] Shi-Jie Cao,[a] Qing-Wen Ye,[b] Jing Bai,*[a] Hua Liu*[c]

[a]*College of New Energy, Yulin University, Shaanxi Province, Yulin 719000, People's Republic China.*

[b]*School of Materials Science and Engineering, Xi'an University of Technology, Xi'an 710048, China*

[c]*College of Chemical Engineering and Technology, Taiyuan University of Science and Technology, Shanxi Province, Taiyuan 030024, People's Republic China.*

CONTENTS

S1. Materials and measurements

All solvents and starting materials for synthesis were purchased commercially and used without further purification. ^{1}H NMR and ^{13}C NMR experiments were performed with a Bruker-AVANCE III 400 MHz spectrometer, using TMS (tetramethylsilane) as an internal standard. MS spectra were performed with Bruker micrOTOF-Q II ESI-Q-TOF LC/MS/MS spectroscopy. Elemental analyses (for carbon, hydrogen, and nitrogen) were taken on a PerkinElmer 2400C elemental analyzer. Fourier-transformed infrared (FTIR) spectra measurements (4000-400 cm^{-1}) were performed with KBr pellets on a Bruker EQUINOX-55 FTIR spectrometer. UV-VIS-NIR spectroscopy measurements were conducted with BaSO$_4$ pellets on a UV-3600PLUS spectrometer. The products phase purity was examined by PXRD in the angular range of $2\theta = 5$-$50°$, using a Bruker D8 ADVANCE X-ray powder diffractometer (Cu Kα, 1.5418 Å). TGA, using Netzsch TG209F3 equipment, was performed under a nitrogen stream with a heating rate of 10 °C min^{-1}. The gas sorption studies were measured by using Micromeritics ASAP 2020 M adsorption equipment. The apparent surface areas were determined from the CO$_2$ adsorption isotherms collected at 195 K by applying the Brunauer-Emmett-Teller (BET). Variable-temperature magnetic susceptibilities were obtained on a Quantum Design MPMS-XL-7 SQUID magnetometer. X-ray photoelectron spectroscopy (XPS) was performed on ULVAC-PHI PHI-5000 VPIII at room temperature. The photocatalytic measurements were conducted on a WP-TEC-1020HSL of WATTCAS photoreactor instrument with different wavelength monochrome LED light-emitting chip. Liquid Ultraviolet-visible (UV-vis) spectra were recorded on a Hitachi-2910 spectrophotometer equipped with a xenon discharge lamp.

Fig. S1 Schematic view of WP-TEC-1020HSL of WATTCAS photoreactor instrument for photocatalytic measurements.

S2. Synthesis

Synthesis of L ligand

The L was synthesized according to the published literature[1]. ^{1}H NMR (400 MHz, TMS, CDCl$_3$) δ 8.98 (d, 4H, J = 4.3 Hz), 8.53 (d, 4H, J = 4.5 Hz) ppm. ^{13}C NMR (100 MHz, TMS, CDCl$_3$) δ 163.46, 151.00, 138.31, 121.08. HRMS (ESI) m/z calcd for $C_{12}H_9N_6^+$ ([M + H]$^+$): 237.0889, found: 237.0881.

Synthesis of {[Co(L)(Hbtc)]·MeOH·DMF}$_n$ (Co(II)-MOF)

A mixture of Co(NO$_3$)$_2$·6H$_2$O (0.075 mmol, 0.0218 g), L (0.075 mmol, 0.0177 g), H$_3$btc (0.05 mmol, 0.0105 g) and DMF/MeOH (3 mL/5 mL) was sealed in a Teflonlined stainless steel vessel (25 mL), heated at 80 ˚C for 3 days. After the mixtures were slowly cooled to room temperature at a rate of 5°C h^{-1}, red block crystals of Co(II)-MOF with 85.6% (based on L) were collected. Anal. Calcd for $C_{23.36}H_{18.65}CoN_{6.79}O_{7.79}$ (578.10 g mol^{-1}): C, 48.49; H, 3.22; N, 16.44 %. Found: C, 48.52; H, 3.18; N, 16.35 %. IR (KBr, cm^{-1}): 3415 w, 1667 m, 1615 m, 1446 m, 1381 s, 1279 w, 1101 w, 717 m.

S3. Crystallography and structural characterization

Table S1. Crystallographic data and structure refinement parameters for Co(II)-MOF.

MOF	Co(II)-MOF
Empirical formula	$C_{23.36}H_{18.65}CoN_{6.79}O_{7.79}$
CCDC	2236021
Formula weight	578.10
Crystal system	Triclinic
Space group	P-1
Temperature (K)	180.0
a (Å)	10.1137(17)
b (Å)	10.5199(19)
c (Å)	13.313(2)
α (°)	100.928(6)
β (°)	94.163(6)
γ (°)	107.181(6)
V (Å^3)	1316.2(4)
Z	2
D_{calc}(g/cm^3)	1.459
F(000)	591
Reflections collected	12897
Independent reflections	4736
R_{int}	0.0530
Number of parameters	411
GOOF	1.184
Final R indices [I>2sigma(I)]	$R_1 = 0.0655$, $wR_2 = 0.1882$
R indices (all data)	$R_1 = 0.0808$, $wR_2 = 0.2119$

$^a R_1 = \sum(||F_o| - |F_c|)/\sum|F_o|$. $^b wR_2 = [\sum w(F_o{}^2 - F_c{}^2)^2/\sum w(F_o{}^2)^2]^{1/2}$

Table S2. Selected bond lengths (Å) and angles (º) for Co(II)-MOF

	Co(II)-MOF		
Co(1)-O(2)#1	2.028(3)	Co(1)-O(3)	2.028(3)
Co(1)-O(4)#2	2.160(3)	Co(1)-O(5)#2	2.225(3)
Co(1)-N(6)	2.140(3)	Co(1)-N(8)#3	2.139(3)
O(2)#1-Co(1)-O(4)#2	154.32(13)	O(2)#1-Co(1)-O(5)#2	94.60(11)
O(2)#1-Co(1)-N(6)	87.40(11)	O(2)#1-Co(1)-N(8)#3	87.69(11)
O(3)-Co(1)-O(2)#1	117.67(11)	O(3)-Co(1)-O(4)#2	87.93(11)
O(3)-Co(1)-O(5)#2	146.86(10)	O(3)-Co(1)-N(6)	88.86(12)
O(3)-Co(1)-N(8)#3	94.82(13)	O(4)#2-Co(1)-O(5)#2	59.75(10)
N(6)-Co(1)-O(4)#2	91.35(11)	N(6)-Co(1)-O(5)#2	85.10(12)
N(8)#3-Co(1)-O(4)#2	92.40(12)	N(8)#3-Co(1)-O(5)#2	93.72(12)
N(8)#3-Co(1)-N(6)#2	174.84(11)		

Symmetric code: #1: $-x$, $-y + 1$, $-z + 2$; #2: $x + 1$, $-y + 1$, $-z + 2$. #3: x, $y + 1$, $z + 1$.

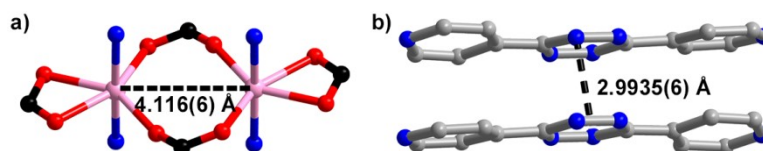**Fig. S2** (a) The Co···Co distance in the $[Co_2(COO)_4N_4]$ clusters; (b) View of the $\pi\cdots\pi$ interactions between the tetrazine and tetrazine rings in Co(II)-MOF.
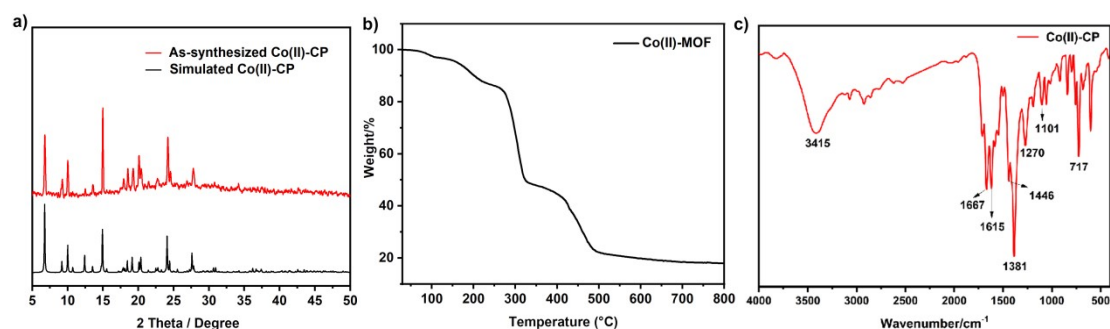

Fig. S3 The PXRD pattern (a), TGA curve (b), and FT-IR spectrum (c) of Co(II)-MOF

S4. Gas adsorption study of Co(II)-MOF

Gas adsorption measurements (N_2, CO_2, and CH_4) were performed. In order to remove the guest molecules in Co(II)-MOF, the higher purity sample Co(II)-MOF was immersed in CH_2Cl_2 for 3 days, and the solvent was changed every 12 hours. Then the sample Co(II)-MOF was subjected to vacuum activation at 130 °C for 6 hours before the adsorption measurements. TG curves before and after sample treatment indicated that the guest molecules (DMF and CH_3OH) in Co(II)-MOF have been removed, and the PXRD pattern showed that the framework of Co(II)-MOF is substantially intact after activation (Fig. S4).
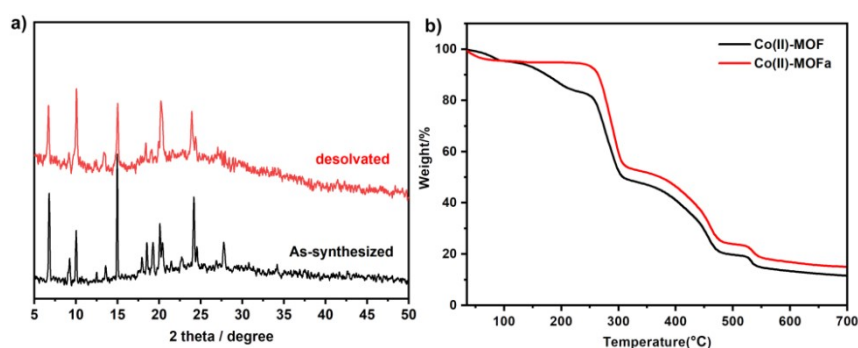
Fig. S4 (a) PXRD curves of Co(II)-MOF and desolvated Co(II)-MOF samples; (b) TGA curves of Co(II)-MOF and desolvated Co(II)-MOFa samples.

The desolvated sample Co(II)-MOFa was subjected to gas adsorption measurements (N_2, CO_2, and CH_4). The sample Co(II)-MOFa show a small amount of N_2 uptake (31.73 $cm^3(STP)g^{-1}$ at 101.325 kPa) at 77 K (Fig. S5a). At 195 K, the uptake amount of CO_2 can reach 45.70 cm^3g^{-1} (8.97 wt%), while that of CH_4 is 13.98 cm^3 g^{-1} (0.99 wt%). When the measured temperature changed to 273 K and 298 K, the uptake amounts of both CO_2 and CH_4 decreased (Fig. S5). The curve analyses reveal that Co(II)-MOFa hardly adsorb CH_4, but adsorb less amount of CO_2 (26.10 cm^3 g^{-1} for 273K and 18.08 cm^3 g^{-1} for 298 K).
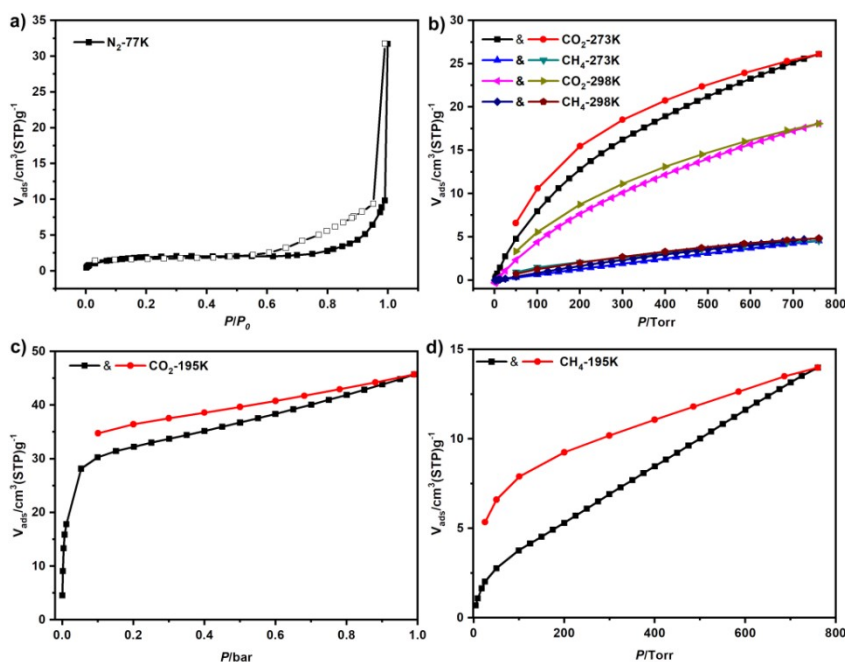
Fig. S5 (a) The N_2 adsorption isotherms of Co(II)-MOFa measured at 77 K; (b) Sorption isotherms of Co(II)-MOFa: CO_2 273 K, 298 K and CH_4 273 K, 298 K; (c) CO_2 sorption isotherms of Co(II)-MOFa at 195 K. (d) CH_4 sorption isotherms of Co(II)-MOFa at 195 K.

To predict CO_2/CH_4 selectivity in Co(II)-MOFa for a CO_2/CH_4 binary mixture, the ideal adsorbed solution theory (IAST) was employed on the basis of the adsorption curves of CO_2 and CH_4. As shown in Fig. S6, for CO_2/CH_4 mixtures with general feed compositions of landfill gas (CO_2/CH_4 = 50/ 50), Co(II)-MOFa exhibits a high initial CO_2/CH_4 selectivity of 32.9, and then the selectivity decreases with increasing pressure to 15.9 at 1 atm at 273K. While at 298K, the initial CO_2/CH_4 selectivity for Co(II)-MOFa is higher at 11.9. As the pressure increases, the selectivity gradually decreases to 7.9, and then rises to 8.9.

To further study the affinity of Co(II)-MOFa for CO_2, the isosteric heat of CO_2 adsorption (Q_{st}) was calculated on the basis of the virial II equation from the CO_2 sorption isotherms at 273 and 298 K (Fig. S7). The equation shows that Q_{st} displays high values of 59.3 kJ mol^{-1} at initial coverage, reflecting strong framework-CO_2 interactions.
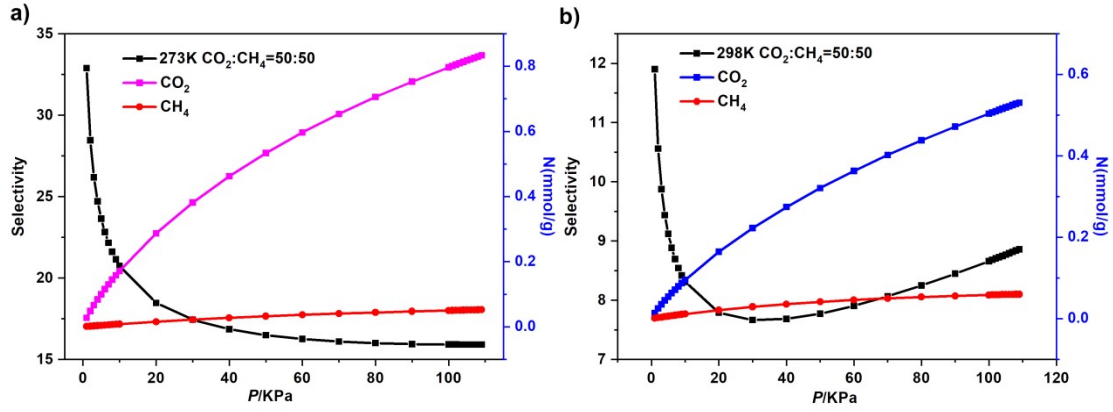
7

Fig. S6 IAST adsorption selectivities of **Co(II)-MOFa** for equimolar mixtures of CO_2 and CH_4.

IAST adsorption selectivity calculation:

The experimental isotherm data for pure CO_2 and CH_4 (measured at 298 K) were fitted using a Langmuir-Freundlich (L-F) model:

$$q = \frac{a_1 * b_1 * P^{1/c1}}{1 + b_1 * P^{1/c1}} + \frac{a_2 * b_2 * P^{1/c2}}{1 + b_1 * P^{1/c1}} \square$$

Where q and p are adsorbed amounts and pressures of component i, respectively. The adsorption selectivities for binary mixtures of CO_2/CH_4, defined by

$$S_{i/j} = \frac{x_i * y_j}{x_j * y_i}$$

were calculated using the Ideal Adsorption Solution Theory (IAST) of Myers and Prausnitz.

Where x_i is the mole fraction of component i in the adsorbed phase and y_i is the mole fraction of component i in the bulk.

Calculation of sorption heat for CO_2 uptake using Virial 2 model

$$\ln P = \ln N + 1 \Big/ T \sum_{i=0}^{m} a_i N^i + \sum_{i=0}^{n} b_i N^i \qquad Q_{st} = -R \sum_{i=0}^{m} a_i N^i$$

Where P is the pressure, N is the adsorbed amount, T is the temperature, a_i and b_i are virial coefficients, and m and n are the number of coefficients used to describe the isotherms. Q_{st} is the coverage-dependent enthalpy of adsorption and R is the universal gas constant.
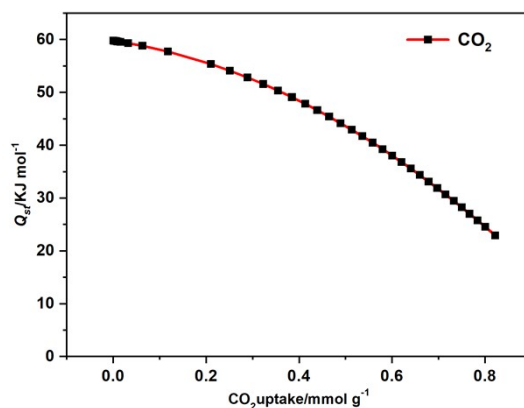
Fig. S7 The isosteric heat of CO_2 adsorption for Co(II)-MOF estimated by the virial equation from the adsorption isotherms at 273 and 298 K.

S5. Chemical stability of Co(II)-MOF

In this work, we examined the thermal stability, water stability, and chemical stability of Co(II)-MOF to estimate its robustness. To evaluate the thermal stabilities of Co(II)-MOF, TGA experiments were conducted from 30 to 700 °C under a nitrogen atmosphere (Fig. S4b). The TGA curve of Co(II)-MOF indicates a weight loss of 5.02% in the temperature range of 30-112 °C, which is consistent with the release of lattice MeOH molecules (calculated 5.26%). Then an obvious weight loss of 12.03% before 230 °C is observed, which corresponds to the removal of lattice solvent DMF molecules (calculated 12.01%). Then the Hbtc^{2-} and L ligands begin to collapse upon further heating until 626 °C. The desolvated samples Co(II)-MOFa were prepared by immersing the as-synthesized samples of Co(II)-MOF in dichloromethane (DCM) for one week, and then heating the immersed samples at 130 °C under vacuum for 8 h to obtain Co(II)-MOFa. The PXRD patterns and TGA curves of Co(II)-MOFa have been tested, and their changes indicate the removal of guest molecules (Fig. S4). The stability experiments are further performed under other harsh conditions. For solvent stability, 10 mg of Co(II)-MOF crystals were soaked in 5 mL different common solvent (1,4-dioxane, MeOH, EtOH, CH_3CN, THF, toluene, DMF, DMA, DMSO, NMP and H_2O) for two weeks (yet H_2O for three months), the recovered powder was further examined by PXRD. And for pH stability, 10 mg of Co(II)-MOF crystals were soaked in 5 mL different pH aqueous solutions (pH 2-12) for two weeks, and the recovered powder was further examined by PXRD.
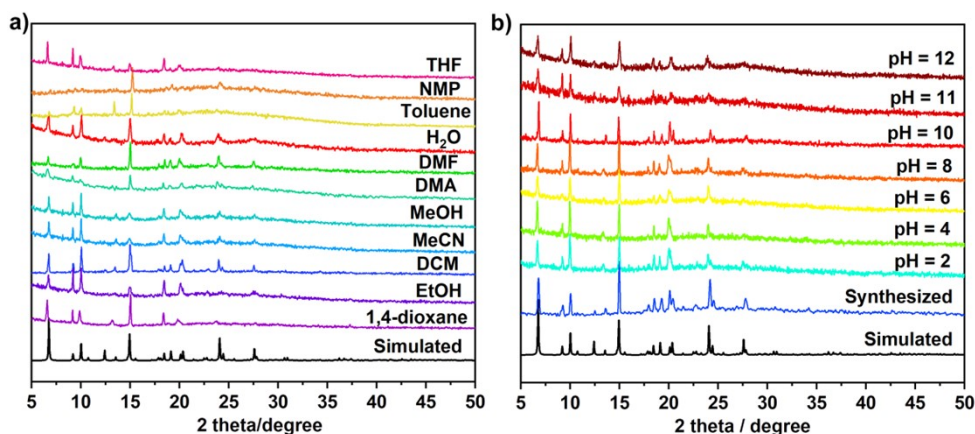
Fig. S8 (a) PXRD patterns of Co(II)-MOF after soaking in various solvents for two weeks; (b) PXRD patterns of Co(II)-MOF after soaking in water of pH from 2 to 12 for two weeks.
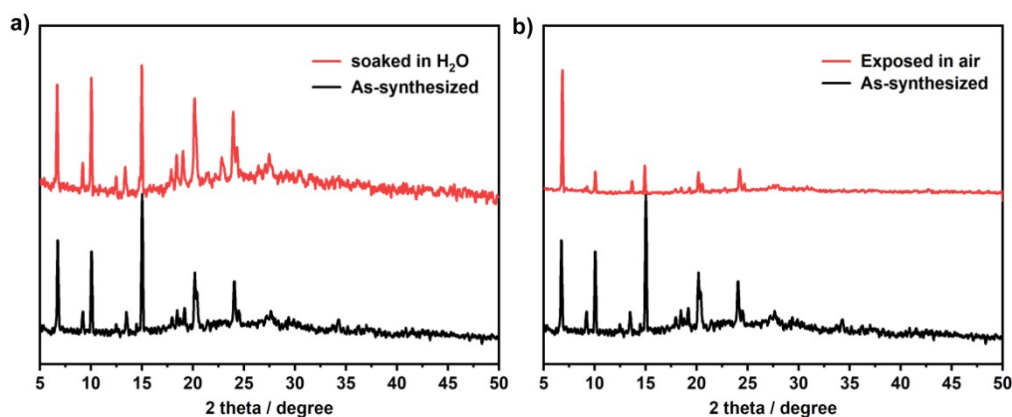

Fig. S9 (a) PXRD patterns of Co(II)-MOF after soaking in H_2O for one year; (b) PXRD patterns of Co(II)-MOF after exposing in air for two years.

S6. Photo-thermo synergistic decomposition of permanganate solution

The photoreactor is a WP-TEC-1020HSL of WATTCAS PCX50A Discover multi-channel photocatalytic reaction system with a power of 10W every light path under light irradiation (with different wavelength LED lamps). The reactor temperature was varied by using heating chassis and a temperature controller. 5 mL of target pollutant aqueous solution was added to a 15 mL cylindrical quartz tube, 10 mg of photocatalyst was ultrasonically dispersed in it for 5 minutes, and magnetically stirred (500 rpm). Before irradiation, the suspension was kept in the dark and stirred for 1 hour to achieve adsorption-desorption equilibrium. In the process of UV-visible light irradiation, 3mL samples were taken at regular intervals and filtered with a 0.22uM filter to remove the solid catalyst. Finally, the concentration of MnO_4^- remaining after degradation were

measured with a UV-vis spectrometer, and their maximum absorption wavelengths were at 525 nm.

Time dependent study of MnO$_4^-$ degradation

We took 5 mL of an aqueous solution of 96 mg/L MnO$_4^-$ solution in a silica tube and recorded the initial absorbance with UV-Vis spectroscopy. To the silica tube, 10 mg of Co(II)-MOF crystals were added, and after several time intervals we recorded the corresponding absorbance spectra of the supernatant solution.

Study of MnO$_4^-$ degradation in the presence of competing anions

Selective experiment: 10 mg of Co(II)-MOF crystals were immersed in 5 ml of 96 mg/L MnO$_4^-$, Cr$_2$O$_4^{2-}$, CrO$_4^{2-}$, and ReO$_4^-$, respectively. The degradation process was monitored by UV-vis spectroscopy at intervals based on the variation of the maximum adsorption peak at 525, 350, 373 and 202 nm, respectively. The samples were collected after 90 minutes for determining the MnO$_4^-$ concentration in the solution using UV-vis spectroscopy.

Competitive experiment: The effects of competing anions and cations on the degradation efficiency were investigated. In this study, we took Cl$^-$, Br$^-$, NO$_3^-$, SO$_4^{2-}$, CO$_3^{2-}$, PO$_4^{3-}$, SO$_3^{2-}$, or I$^-$ as the competing anions, and Mg^{2+}, Ni^{2+}, Co^{2+}, Zn^{2+}, Ca^{2+}, Na$^+$, or Cd^{2+} as the competing cations, which are omnipresent in common water sources and waste waters. 10 mg of Co(II)-MOF crystals were added in 5 ml of 96 mg/L MnO$_4^-$ solution in the presence of 10-fold of each competing ion with photo-catalysis. The samples were collected after 90 minutes for determining the MnO$_4^-$ concentration in the solution using UV-Vis spectroscopy.

Recyclability test of Co(II)-MOF catalyst

After first photocatalytic degradation measurement, recycle tests were executed. And after each cycle, the solid catalyst was filtrated and washed for several times to remove the left pollutants by using distilled water and ethanol, and then dried at 60 ^{o}C overnight for PXRD measurements.
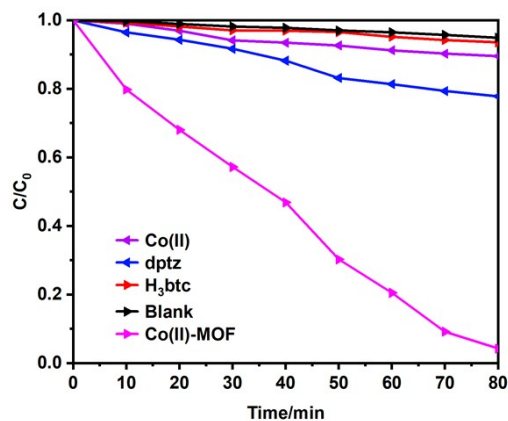
Fig. S10 The control experiments for the degradation of MnO_4^- utilizing different catalysts under the UV irradiation.
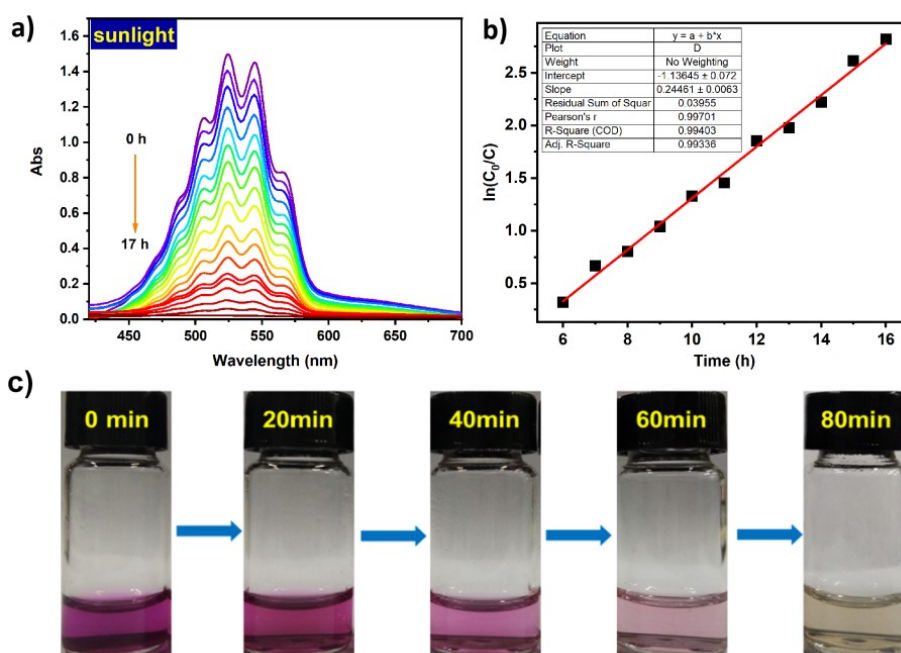

Fig. S11 (a) The UV-vis spectra used to monitor the MnO_4^- concentration at various time points with the catalyst Co(II)-MOF under sunlight condition; (b) The the rate of MnO_4^- degradation reaction catalyzed by Co(II)-MOF under sunlight irradiation was calculated by adopting the pseudo-first-order kinetic equation; (c) The corresponding color changes of MnO_4^- solution with the catalyst Co(II)-MOF under 465 nm irradiation condition.
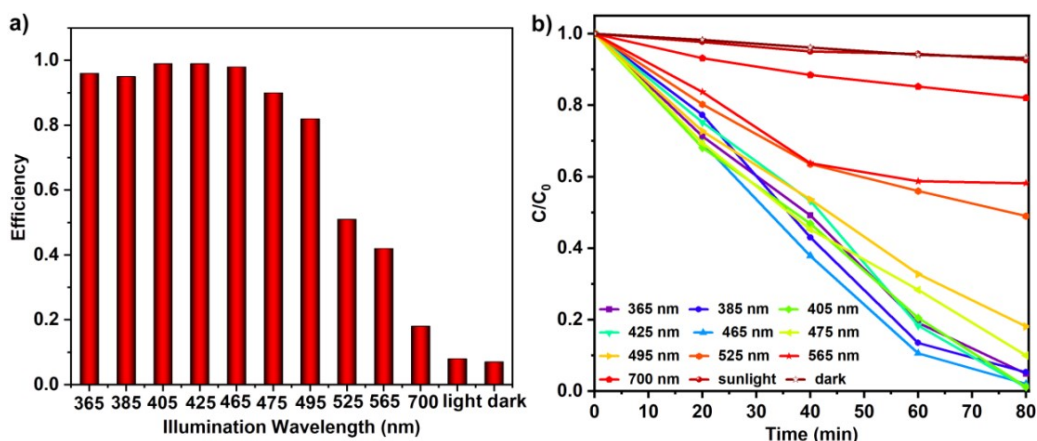
Fig. S12 (a) The bar diagrams represent the catalytic activity of Co(II)-MOF at different wavelengths irradiation at 80 min; (b) The photo-catalytic degradation efficiency in different wavelengths irradiation.
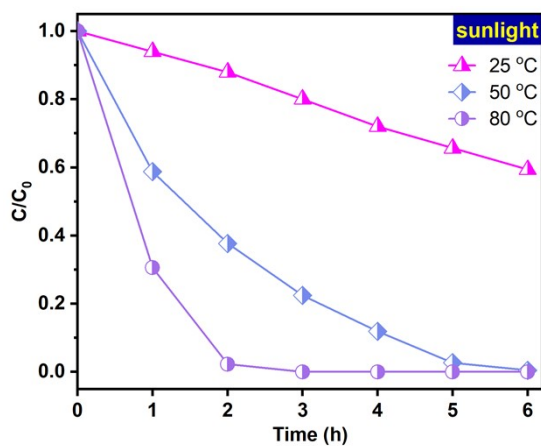
Fig. S13 The effect of temperature for the catalytic activity of Co(II)-MOF (a) in dark, (b) sunlight and (c) 465 nm illumination source conditions.
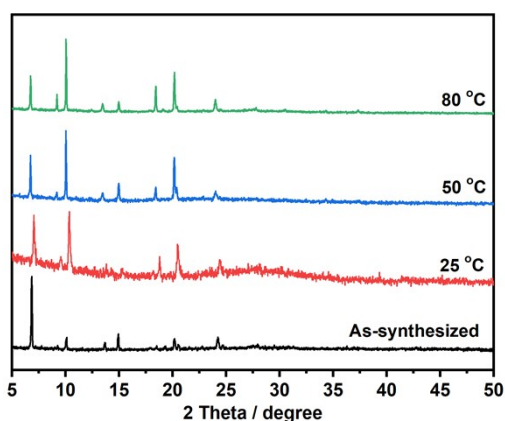

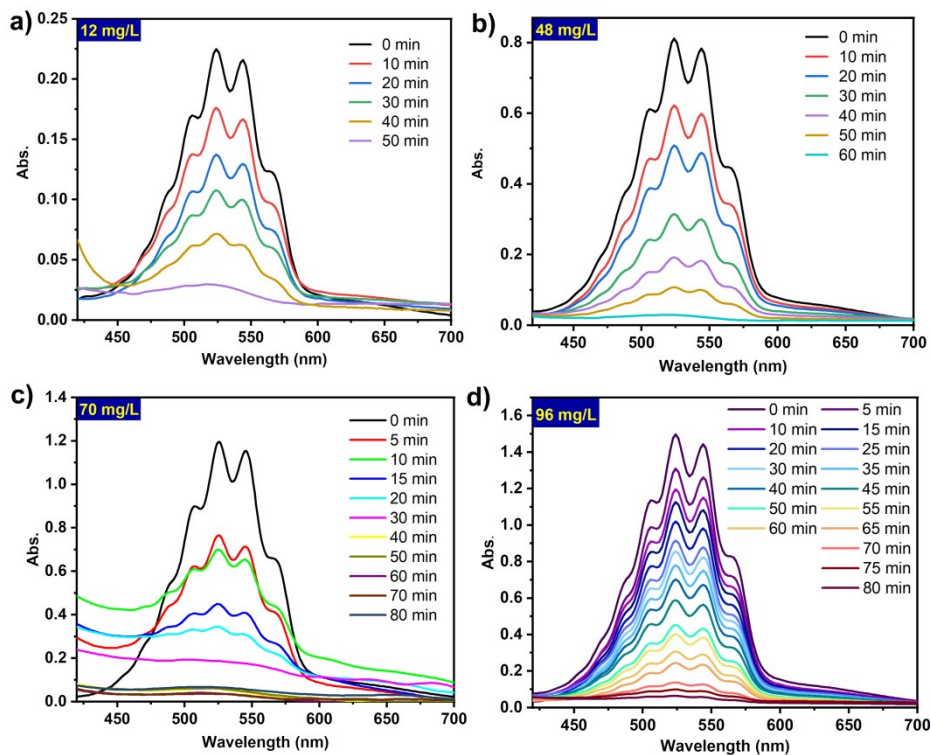**Fig. S14** PXRD patterns of Co(II)-MOF after photocatalytic degradation in different temperature.

Fig. S15 The photo-degradation performances of Co(II)-MOF (10 mg) towards the various concentration of MnO_4^- (12, 48, 70 and 96 mg/L).
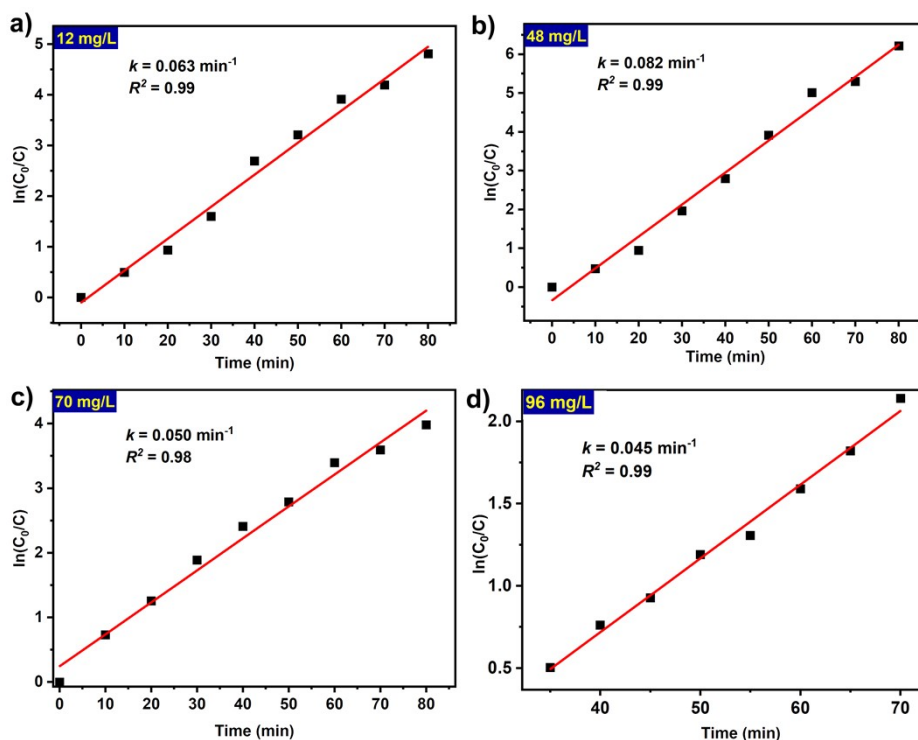
Fig. S16 The the rate of MnO_4^- degradation reaction catalyzed by Co(II)-MOF (10 mg) towards the various concentration of MnO_4^- (12, 48, 70 and 96 mg/L).
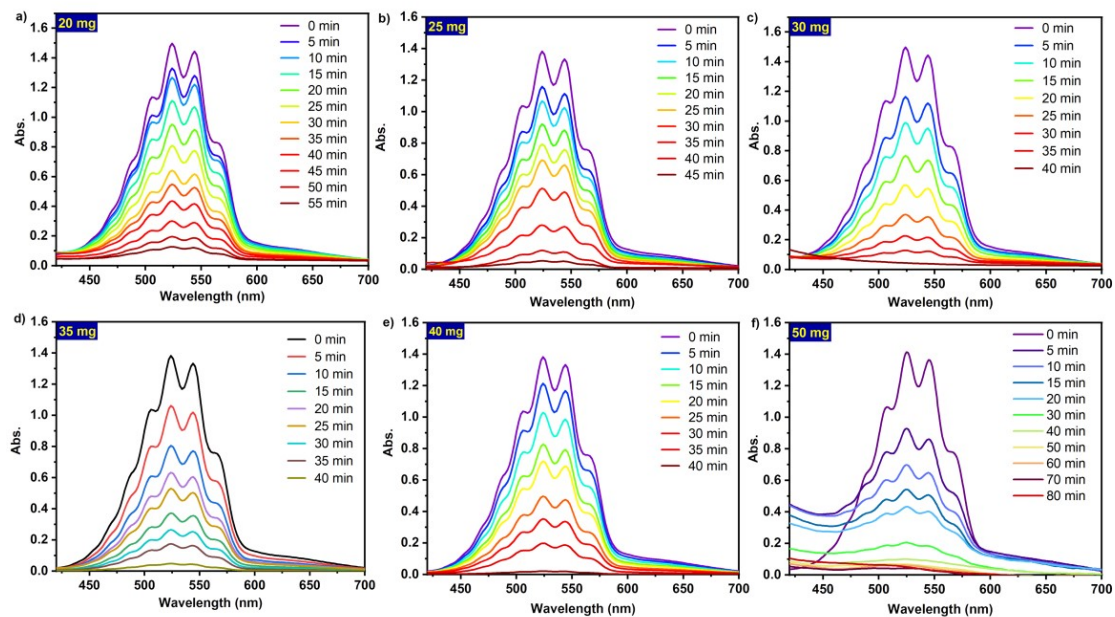
Fig. S17 The 96 mg/L MnO_4^- photo-degradation with the catalyst amount being 20, 25, 30, 35, 40 and 50 mg.
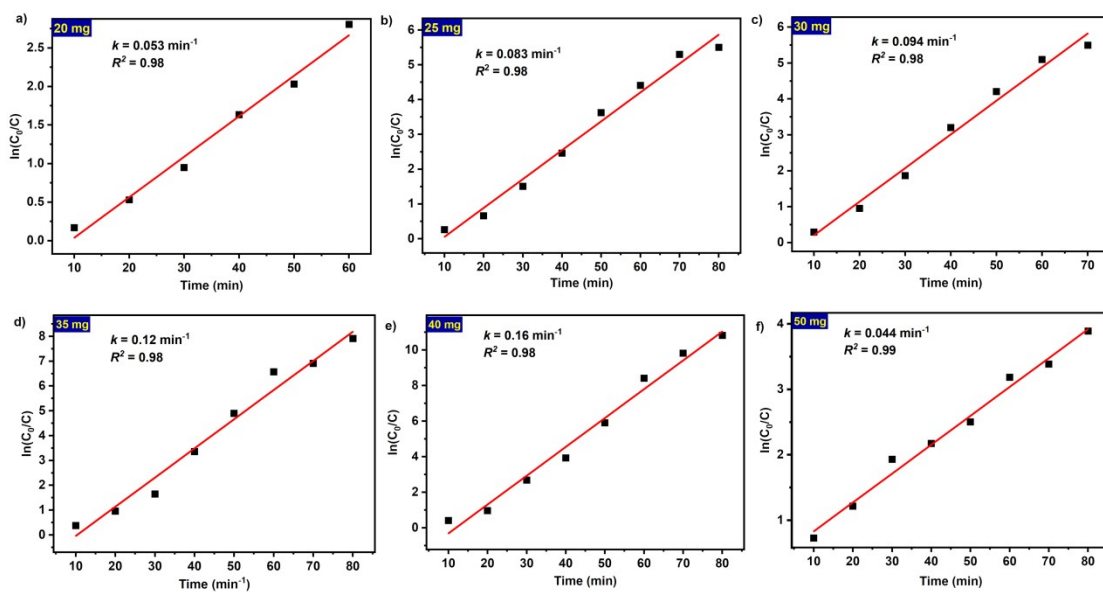

Fig. S18 The the rate of MnO_4^- degradation reaction catalyzed by Co(II)-MOF towards the various amounts of catalyst (20, 25, 30, 35, 40 and 50 mg).
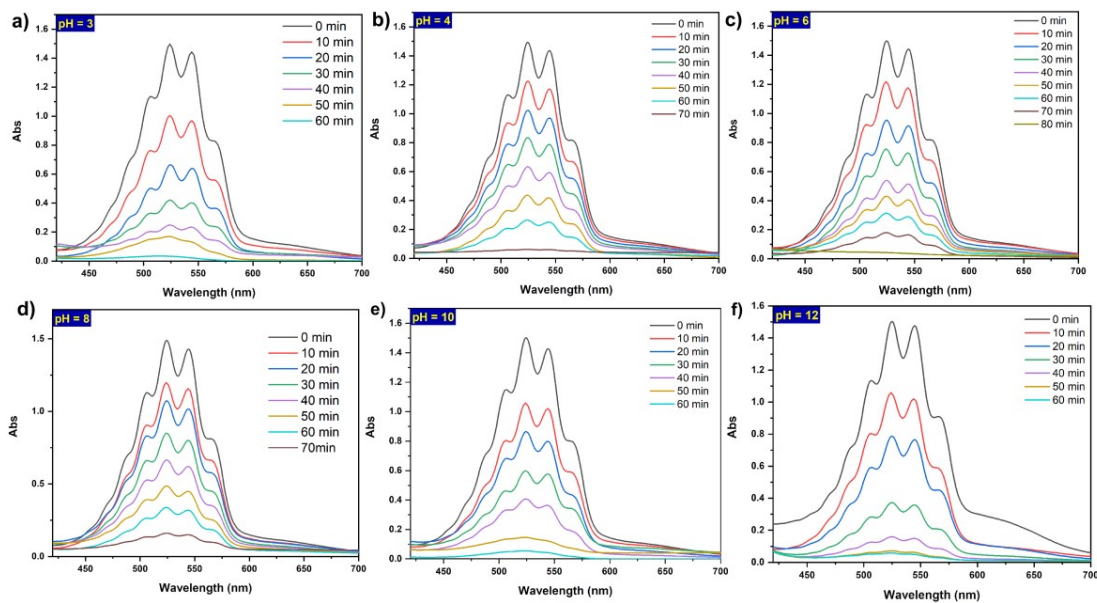
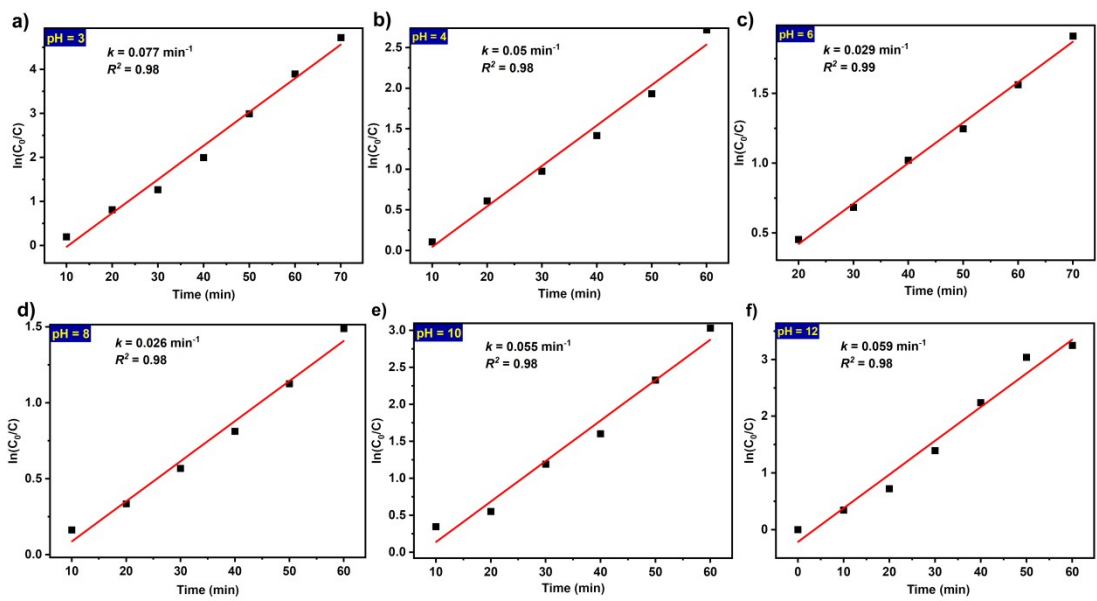**Fig. S19** The 96 mg/L MnO_4^- photo-degradation solution with various pH.

Fig. S20 The the rate of MnO_4^- degradation reaction catalyzed by Co(II)-MOF with various pH.
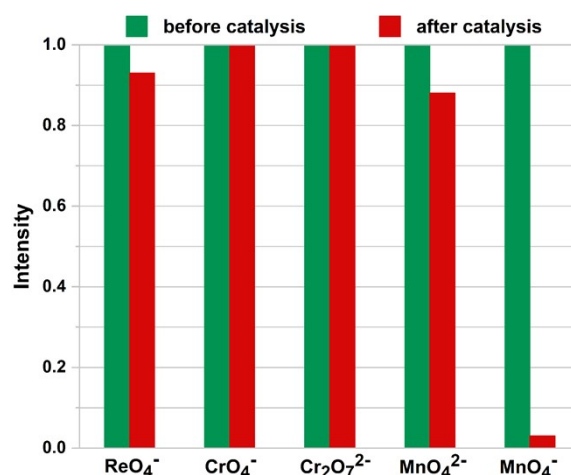
Fig. S21 The bar diagrams represent the degradation of ReO_4^-, CrO_4^{2-}, $Cr_2O_7^{2-}$, MnO_4^{2-}, and MnO_4^- with Co(II)-MOF.
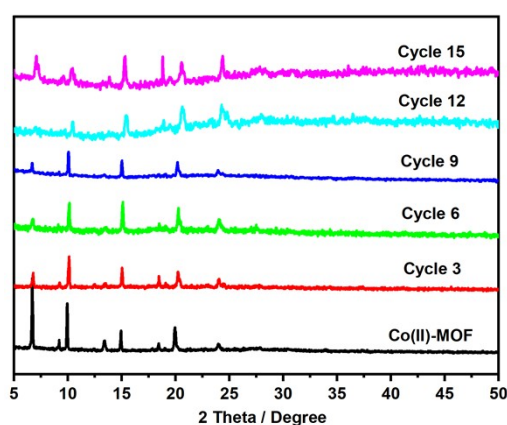

Fig. S22 PXRD patterns of Co(II)-MOF after recycling measurements.

S7. Photocatalytic decoloration of Methyl Orange

In addition to MnO_4^-, the degradation of other organic dyes were also investigated by utilizing Co(II)-MOF. Here, the methyl orange (MO), methylene blue (MB), methylene green (MG), congo red (CR), malachitegreen oxalate (MGO) and rhodamine B (RhB) were selected as model dye contaminants for degradation experiments, which are commonly present in industrial wastewater. 5 mg powder of the title MOF were dispersed in the MO, MB, MG, CR, MGO and RhB solution (3×10^{-5} mol L^{-1}), respectively, magnetically stirred in the dark for 0.5 h to ensure the adsorption-desorption equilibrium of the working solution. After the UV irradiation, it was shown that obvious and quick decoloration was observed for MO, yet the color of other dyes

17

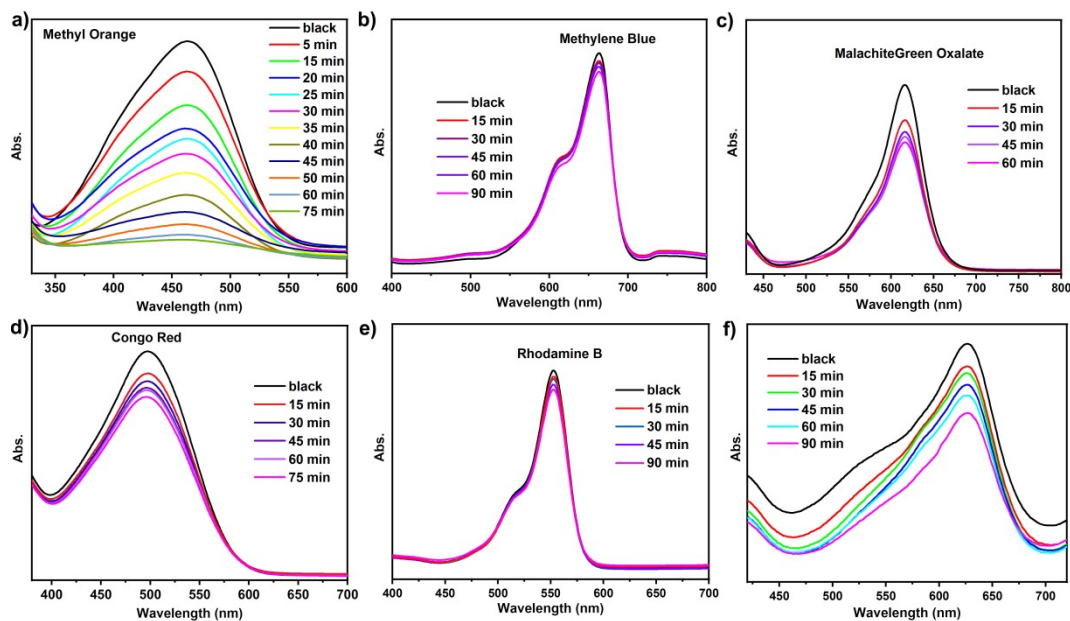remain substantially unchanged, indicating that Co(II)-MOF displays good selective photodegradation towards MO.

Fig. S23 UV-vis spectra used to monitor the dye concentration at various time points with the catalyst Co(II)-MOF.
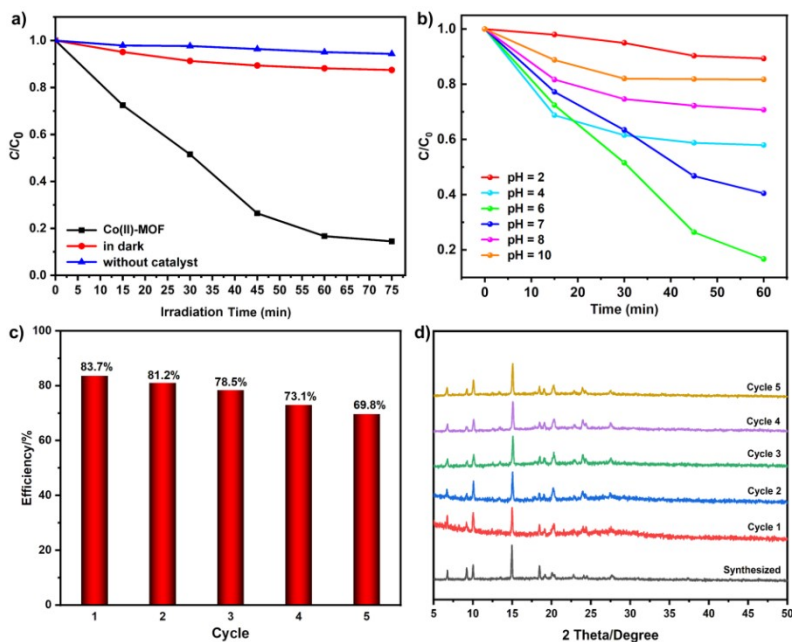

Fig. S24 (a) The control experiments concerning the MO degradation with or without catalysts in the dark or UV irradiation conditions; (b) The decoloration of MO solution with various pH catalyzed by Co(II)-MOF under UV irradiation; (c) Recycled performance of Co(II)-MOF for degradation of MO. (d) PXRD patterns of Co(II)-MOF after recycling measurements.

The photocatalytic degradation in aqueous solutions of Co(II)-MOF towards MO was further explored. Approximately 85.6% decoloration efficiency for MO was observed at 75 min, and the rate of degradation reaction was 0.86 h^{-1}, which was calculated by adopting the pseudo-first-order kinetic equation according to the Langmuir-Hinshelwood model. Besides, control experiments on the photodegradation of MO were also carried out in the dark or without catalyst, and it showed that Co(II)-MOF is active for the decomposition of MO in the presence of UV irradiation. Furthermore, the photocatalytic performance of Co(II)-MOF towards the decoloration of MO aqueous solution with various pH (adjusted by 0.1 M HCl and NaOH) were also investigated. The MO degradation efficiency followed the order of pH = 6 (84 %) > pH = 7 (60 %) > pH = 4 (42 %) > pH = 8 (29 %) > pH = 10 (18 %) > pH = 2 (11 %) at 60 min, and the strong acid and base were likely to prejudice the degradation of MO, and the optimal is at pH = 6.

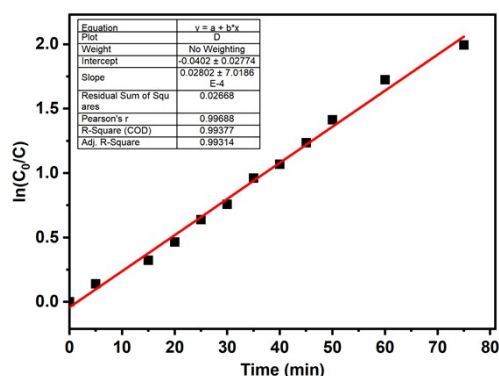| Equation | y = a + b*x |
Plot	D
Weight	No Weighting
Intercept	-0.0402 ± 0.02774
Slope	0.02802 ± 7.0186 E-4
Residual Sum of Squares	0.02668
Pearson's r	0.99688
R-Square (COD)	0.99377
Adj. R-Square	0.99314

Fig. S25 The the rate of MO degradation reaction catalyzed by Co(II)-MOF under UV irradiation was calculated by adopting the pseudo-first-order kinetic equation according to the Langmuir-Hinshelwood model.
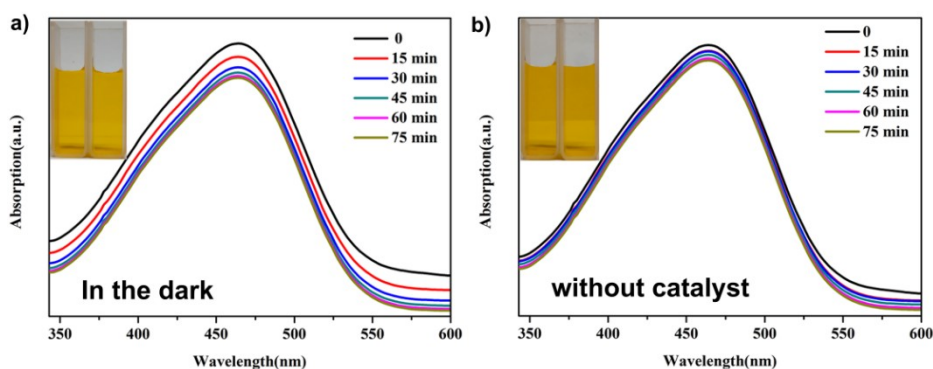

Fig. S26 (a) The MO removal experiment catalyzed by Co(II)-MOF in the dark condition; (b) The MO removal experiment without catalysts under UV irradiation.

Furthermore, the stability and recyclability of Co(II)-MOF towards the decoloration of MO were also explored. As the number of photocatalytic cycles increases, the degradation efficiency of Co(II)-MOF to MO is only slightly reduced. After the 5th run, the photocatalytic degradation efficiency still reached 69.8%, showing a reliable photocatalytic recycling capacity, and a slight decrease in the photodegradation efficiency is most likely due to a small loss of catalyst during actual repetitive operations. Moreover, the recovered solid photocatalyst remained its framework integrity, presenting the good recyclability of Co(II)-MOF towards the photodegradation of MO.
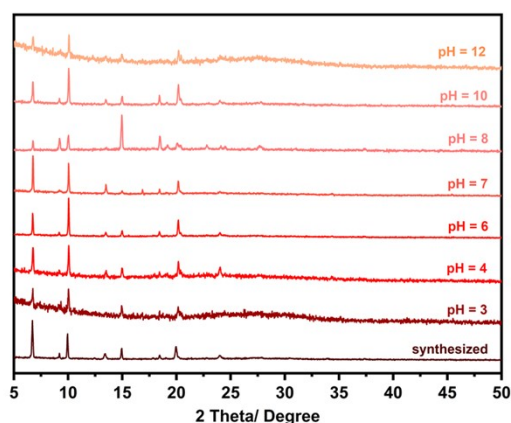

Fig. S27 The PXRD patterns of Co(II)-MOF after photocatalytic degradation in various pH.
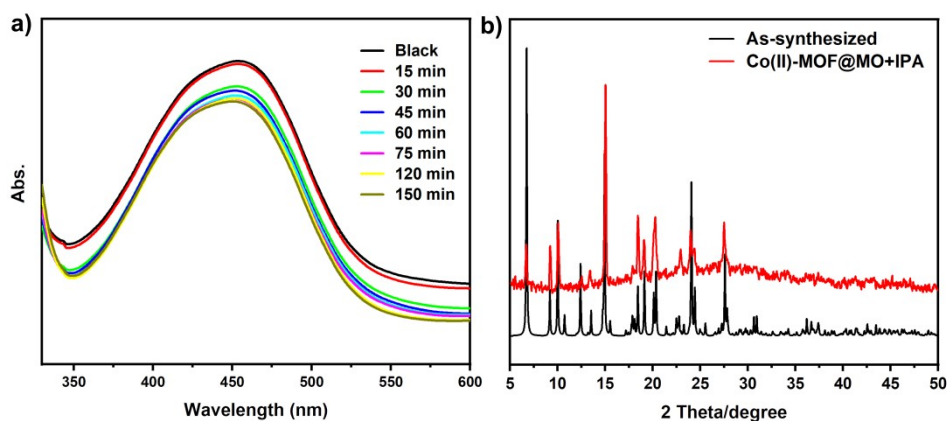

Fig. S28 (a) Effect of IPA scavenger for hydroxyl radicals on photodegradation efficiency of MO using Co(II)-MOF; (b) Effect of IPA scavenger for the integrity of Co(II)-MOF framework.

Moreover, the photodegradation mechanism of MO catalyzed by Co(II)-MOF was also examined. Generally, hydroxyl radicals ($\cdot$OH) are considered to be one of the main reactive species formed during photocatalytic degradation of organic pollutants. Therefore, the detection of generated $\cdot$OH in the photocatalytic process was carried out

using isopropyl alcohol (IPA) as a˙OH scavenger. It can be observed that the degradation of MO was significantly affected by the addition of 2 mL IPA, and the degradation efficiencies of Co(II)-MOF with IPA for degradation of MO only reached 14.5%. Accordingly, combined with the above discussion, the possible photocatalytic mechanism for degradation of MO with the photocatalysts was proposed. First, the Co(II)-MOF is excited by UV irradiation and the electron-hole pairs are formed. During this process, water molecules can be oxidized by the holes to generate hydroxyl radicals. Meanwhile, the conduction band electrons can react with oxygen to form superoxide radicals, which might be translated into hydroxyl radicals by reacting with water. The produced hydroxyl radicals then decompose the organic dyes.

References

1.   Yang, J.; Karver, M. R.; Li, W.; Sahu, S.; Devaraj, N. K., Metal-Catalyzed One-Pot Synthesis of Tetrazines Directly from Aliphatic Nitriles and Hydrazine. *Angewandte Chemie International Edition* 2012, *51* (21), 5222-5225.